Available online at www.sciencedirect.com
ScienceDirect
Trans. Nonferrous Met. Soc. China 35(2025) 1570−1584

Transactions of
Nonferrous Metals
Society of China
www.tnmsc.cn

Cavitation erosion behavior of $Fe_{50}Mn_{30}Co_{10}Cr_{10}$ high entropy alloy coatings prepared by laser melting deposition

Guo-cheng LIU[1,2,3], Jian-jiang LI[1,2,3], Ning HU[1,2,3], Qi-yong TU[1,2,3], Ze-qi HU[1,2,3], Lin HUA[1,2,3]

1. Hubei Key Laboratory of Advanced Technology for Automotive Components,
Wuhan University of Technology, Wuhan 430070, China;
2. Hubei Collaborative Innovation Center for Automotive Components Technology,
Wuhan University of Technology, Wuhan 430070, China;
3. School of Automotive Engineering, Wuhan University of Technology, Wuhan 430070, China

Received 26 August 2023; accepted 1 April 2024

Abstract: In order to reveal the cavitation erosion mechanisms of $Fe_{50}Mn_{30}Co_{10}Cr_{10}$ coating prepared by laser melting deposition (LMD) technique, the phase composition evolution, microstructure, microhardness, cavitation erosion resistance and failure mechanisms were investigated. The results demonstrate that the amount of martensite HCP ε phase of the coating surface increased by a factor of 2.43, and the microhardness increased from HV 270 to HV 410 after 20 h of cavitation erosion test in distilled water. The cumulative volume loss of the coating was approximately 55% less than that of $AlCoCr_xCuFe$ (x=2.0), and the cumulative mean depth of erosion (MDE) was 9% that of $FeCoCrAlNiTi_x$ (x=2.0). The surface strength and plasticity of the coating were further strengthened in the process of cavitation erosion due to the back stress strengthening and work hardening mechanism caused by the heterogeneous structure, which effectively improved the cavitation erosion resistance of the coating.

Key words: cavitation erosion; $Fe_{50}Mn_{30}Co_{10}Cr_{10}$ high entropy alloy; transformation induced plasticity; laser melting deposition; failure mechanisms

---

1 Introduction

Cavitation erosion is the mechanical degradation of the surface as a consequence of continuous collapse of cavities or bubbles in a surrounding liquid, which often occurs in ship propellers, rudder blades, turbine impellers, pumps and other hydraulic machinery parts [1,2]. The high speed running of hydro-mechanical devices tends to reduce the liquid local pressure and form bubbles or cavities. When these bubbles encounter higher local pressures, they will implode to produce microjets or shock waves, which produce concentrated mechanical loads on the material surface [3−5]. This leads to severe localized plastic deformation and pitting which eventually cause material failure. It is generally accepted that cavitation erosion is a serious threat to the safe operation of underwater equipment. The typical metal loss of the turbine runner due to cavitation is reported to be 5×10^{-4} kg/(m^2·h), and after a few years of operation, the loss is about 200 kg [2,6]. Among the built hydropower stations in China, 40% of the turbines have serious synergistic effects of cavitation and sediment erosion [7], which reduces the efficiency and life of the turbines and increases the operation and maintenance costs, ultimately leading to huge

---

Corresponding author: Guo-cheng LIU, Tel: +86-27-87858200, E-mail: liugch@whut.edu.cn;
Lin HUA, Tel: +86-27-87858200, E-mail: hualin@whut.edu.cn

https://doi.org/10.1016/S1003-6326(25)66768-9

economic losses. Therefore, increasing the cavitation erosion resistance of the hydraulic machinery overcurrent element has great economic value.

Furthermore, cavitation erosion resistance, like corrosion resistance and wear resistance, is a surface phenomenon and is principally determined by the surface properties of a material rather than by the bulk properties [8,9]. Therefore, preparing surface coatings on the metal components is an effective way to improve the cavitation erosion resistance of materials. Various anti-cavitation erosion materials or coatings have been synthesized using different techniques and are widely utilized on hydro-mechanical components [8−17]. High-strength hard coatings, such as WC−Co composite coatings [18], CrN or TiN ceramic coatings [19,20], and FeB diffusion coatings [6], are usually applied to anti-cavitation erosion. These coatings can enhance surface hardness, prevent the substrate from ductile fracture, and improve cavitation erosion resistance to a certain extent. However, harder materials generally have lower toughness and less elastic−plastic deformation. When cavitation erosion occurs, the impact energy of the hard coating surface cannot be dissipated in time under the impact of continuous high-speed microjet, and uncontrollable crack propagation is prone to occur. Therefore, materials with excellent cavitation erosion resistance should have both high deformation strength and excellent toughness, i.e., strength−toughness balance. High strength is utilized to resist deformation during cavitation erosion, and excellent toughness can dissipate energy and prevent premature crack initiation [21].

Recently developed high entropy alloys (HEAs) based on equimolar or near equimolar components with multiple primary elements represent a new paradigm for structural materials [22−26]. Their unique high entropy effect, severe lattice distortion effect, sluggish diffusion effect and cocktail effect provide excellent properties that are unmatched by conventional alloys, such as high strength [27], high hardness [28], high wear and corrosion resistance [25,29−31], and resistance to high temperature oxidation [32]. In recent years, some scholars introduced high entropy alloy materials to prepare anti-cavitation erosion coatings, and have achieved good results. ZHANG et al [9] synthesized FeCoCrAlNi high-entropy alloy coatings on 304 stainless steel by laser surface alloying to improve its corrosion and cavitation erosion resistance. The results demonstrate that the microhardness of the FeCoCrAlNi coating is 3 times that of 304 stainless steel and the cavitation erosion resistance is 7.6 times that of 304 stainless steel. NAIR et al [14] reported the cavitation erosion behavior of $Al_{0.1}CoCrFeNi$ in two different media: distilled water with and without 3.5 wt.% NaCl. Due to the high work-hardening properties and stable passivation film on the surface, the resistance to cavitation erosion and corrosion is significantly improved compared with SS316L steel.

$Fe_{50}Mn_{30}Co_{10}Cr_{10}$ is a transformation-induced plasticity-assisted, dual-phase high-entropy alloy (TRIP-DP-HEA) with high strength and high toughness [24,33]. It has both face-centered cubic (FCC) γ phase and hexagonal close-pecked (HCP) ε phase. At the same time, twinning induced plasticity (TWIP) and transformation induced plasticity (TRIP) overcome the strength−ductility trade-off. NIU et al [34] prepared $Fe_{50}Mn_{30}Co_{10}Cr_{10}$ by laser melting deposition (LMD). The results indicate that the as-printed HEA specimens are dominated by FCC γ phase, plate and needle-like HCP ε phase and exhibits anisotropic mechanical properties, together with the maximum ultimate tensile strength of 760 MPa and maximum elongation of 28%. SUN et al [32] investigated the high temperature tribological properties of dual-phase $Fe_{50}Mn_{30}Co_{10}Cr_{10}$ prepared by the laser melting deposition process and found that it has great high-temperature wear resistance. The average friction coefficient and wear rate of the HEA are respectively 38.6% and 81.6% lower than those at room temperature.

Previous studies have indicated that $Fe_{50}Mn_{30}Co_{10}Cr_{10}$ has not only high strength but also good plasticity, reaching a strength−ductility trade-off. Therefore, $Fe_{50}Mn_{30}Co_{10}Cr_{10}$ has great application potential in anti-cavitation erosion coating. In this work, the cavitation erosion behavior of the $Fe_{50}Mn_{30}Co_{10}Cr_{10}$ coating, prepared by the LMD technique, was systematically studied by ultrasonic cavitation erosion test in distilled water. The cavitation erosion resistance of $Fe_{50}Mn_{30}Co_{10}Cr_{10}$ coating was evaluated by cumulative volume loss, cavitation erosion rate, the mean depth of erosion (MDE) and the mean depth of erosion rate (MDER). Meanwhile, these indices were compared with the results of materials and protective coatings commonly utilized in hydraulic machinery. To reveal the mechanisms of cavitation erosion, the phase composition evolution, microstructure, microhardness, cavitation erosion resistance and failure mechanisms have been investigated.

2 Experimental

2.1 Materials and specimen preparation

The $Fe_{50}Mn_{30}Co_{10}Cr_{10}$ powders with particle size of 45−105 μm were produced by the gas atomization of Fe, Mn, Co and Cr (99.99% in purity) in Ar atmosphere. As-received AISI 304 steel plate was utilized as the substrate material. The nominal compositions of $Fe_{50}Mn_{30}Co_{10}Cr_{10}$ and AISI 304 steel are listed in Table 1.

Table 1 Chemical compositions of $Fe_{50}Mn_{30}Co_{10}Cr_{10}$ HEA and AISI 304 steel (at.%)

Material	C	Si	Cr	Mn	Ni	P	S	Fe	Co
AISI 304 steel	0.08	1.0	19.0	2.0	11.0	0.035	0.03	Bal.	–
Fe50Mn30Co10Cr10	–	–	9.68	29.81	–	–	–	49.86	10.65

Fabrication of the $Fe_{50}Mn_{30}Co_{10}Cr_{10}$ coatings on AISI 304 steel plate was performed using an LDM16080 system from Nanjing Zhongke Yuchen Laser Technology Co., Ltd. (China). The LMD processing is depicted in Fig. 1. The laser scanning direction had a zigzag pattern. The powder was delivered by coaxial blown powder equipment at a rate of 3 g/min with argon carrier gas at a flow rate of 20 L/min. Argon shielding gas with a flow rate of 20 L/min was utilized at the bottom of the nozzle to protect the laser optics. The height of the deposition block was 10 mm. Specimens for the cavitation erosion test were machined from the deposition blocks after the LMD processing.

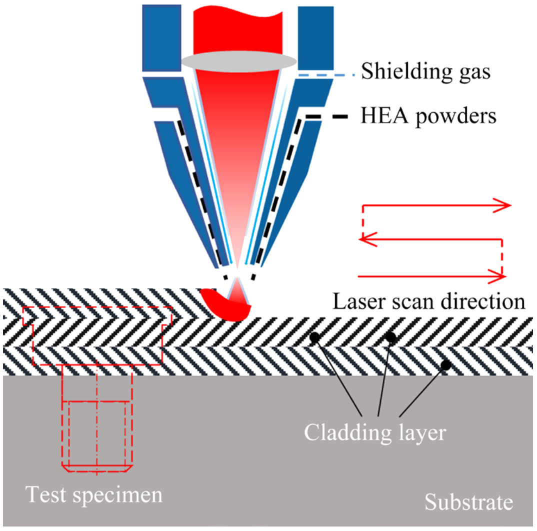

Fig. 1 Schematic diagram of laser melting deposition processing

2.2 Cavitation erosion test

Cavitation erosion tests were conducted on an ultrasonic vibratory apparatus in accordance with the ASTM G32-16(2021) e1 standard. The frequency of vibration resonated at 20 kHz and the amplitude of the horn was 50 μm peak-to-peak. A schematic illustration of the equipment is presented in Fig. 2(a). Test specimens (Fig. 2(b)) were attached to the vibrating horn by screw thread connection. The bottom of the test sample was immersed in distilled water to a depth of about 15 mm. The test medium was maintained at a constant temperature of 25 °C by a circulatory cooling system. Cavitation erosion tests lasted for 20 h, and the mass losses were measured at regular intervals. The mass change was converted to the corresponding volume loss using the density values. Cumulative volume loss, cavitation erosion rate, the mean depth of erosion (MDE, D_E) and the mean depth of erosion rate (MDER, D_R), were also calculated from the mass loss results after cavitation erosion tests. MDE (μm) and the MDER (μm/h) were calculated by the following equations:

$$D_E=\frac{\Delta W}{10\rho A} \tag{1}$$

$$D_R=\frac{\Delta W}{10\rho A\Delta t} \tag{2}$$

where ΔW is the mass loss in mg, ρ is the density of the coating in g/cm^3, A is the eroded area in cm^2, and Δt is the time interval in h.

2.3 Characterization methods

The microstructure of $Fe_{50}Mn_{30}Co_{10}Cr_{10}$ coating, in the as-deposited form, was characterized by a range of techniques. After the LMD process, the specimens were polished with a set of abrasive papers (grit 400−2000) and then cloth polished with diamond polishing agent containing 2.5 μm

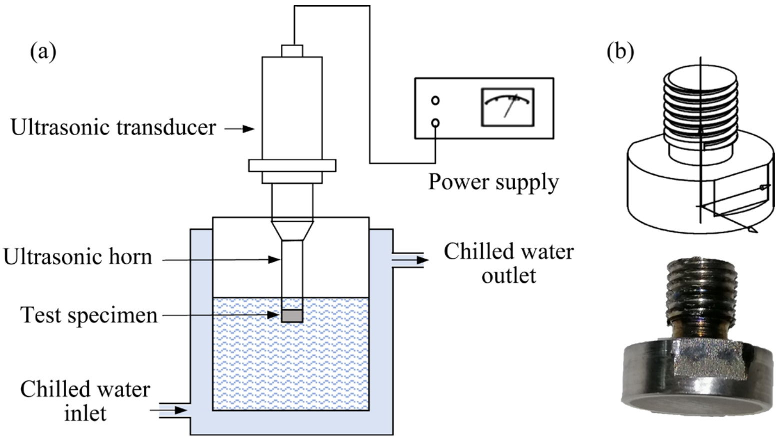

Fig. 2 Schematic diagram of cavitation erosion test: (a) Ultrasonic cavitation erosion device; (b) Test specimen

particles. The specimens were subsequently etched with $FeCl_3$ solution. The microstructural characterization of $Fe_{50}Mn_{30}Co_{10}Cr_{10}$ coating was observed by scanning electron microscope (SEM). The phase analysis was examined by X-ray diffraction (XRD) with Cu K_α radiation (λ=0.15406 nm) at 40 kV and 40 mA. The sample was scanned over a scattering angle range of $30° < 2\theta < 90°$ with a scanning speed of 4 (°)/min. Electron backscattering diffraction (EBSD) was applied to analyzing the crystal orientation and phase content distribution.

After 5, 10, 15 and 20 h of cavitation erosion test, the micromorphology of eroded surfaces was investigated by the SEM, and the microhardness of eroded surfaces was measured by a Vickers hardness tester (HV, Huayin, HV−100A) with a load of 200 g and a duration time of 10 s. After the 20 h test, the surface roughness, R_a and R_{sk} (skewness), were measured by laser scanning confocal microscope (Olympus−OLS4100). In the center of the eroded surface, three measurements were made at horizontal, vertical and oblique, and the measured area was 640 μm × 640 μm. Subsequently, the rough superficial zone of eroded surfaces (40−45 μm from eroded surfaces to the observed area) was polished with abrasive papers and cloth. XRD and EBSD were applied to analyzing the changes in the phase content distribution and crystal orientation. The composition and bonding state of surface layers were determined using X-ray photoelectron spectroscopy (XPS). XPS studies were carried out on an ESCALAB 250 Xi system that employed an Al K_α X-ray source (150 W, 20 eV pass energy, 500 μm spot size). Spectra were analyzed using Thermo Scientific Avantage software and were calibrated with respect to adventitious carbon (the C1 speak) at a binding energy of 284.6 eV. Peaks from survey scans and regional scans were identified with reference to a standard XPS database.

3 Results and discussion

3.1 Cavitation erosion behavior

Figure 3 displays the cavitation erosion behavior of $Fe_{50}Mn_{30}Co_{10}Cr_{10}$ coating with 20 h of test in distilled water. The cavitation erosion process is generally divided into three stages. The first stage is the incubation period with little material loss, followed by the acceleration stage when the material loss is accelerated, and the last stage is the stationary stage with stable material loss. In order to compare the cavitation erosion resistance with that of other materials, the cavitation erosion behavior data of AISI 304 steel [35], $AlCoCr_xCuFe$ coating [35] and $FeCoCrAlNiTi_x$ coating [8] measured in distilled water were cited from previous literature. As seen in Figs. 3(a, b), AISI 304 steel and $AlCoCr_xCuFe$ (x=2.0) coating underwent a quick acceleration stage of cumulative volume loss and erosion rate after a brief incubation period, and after 5 h, they entered a stationary stage of cavitation erosion rate. However, the cumulative volume loss of $Fe_{50}Mn_{30}Co_{10}Cr_{10}$ coating over the first 6 h was quite tiny and then maintained a low growth rate. Meanwhile, the cavitation erosion rate kept a gentle growth until it stabilized, without obvious acceleration period. After 20 h of test, its

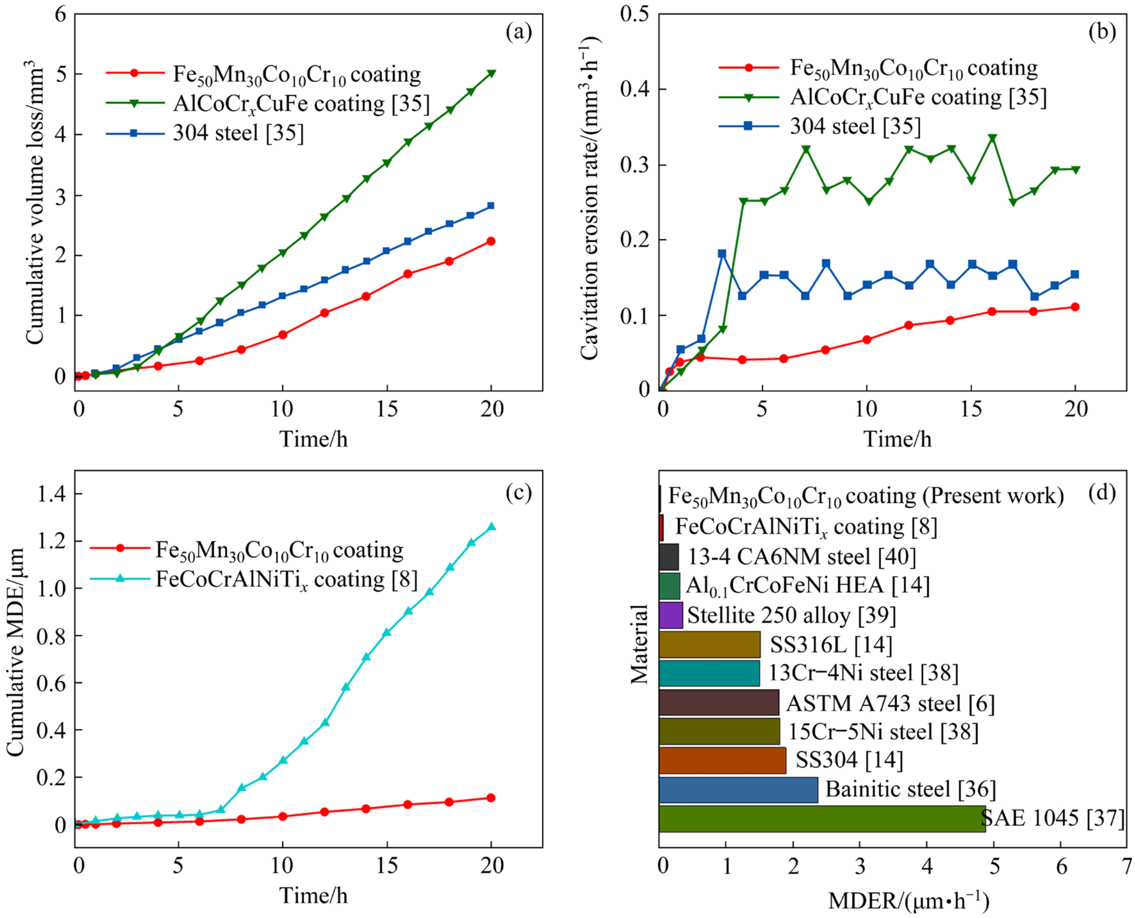

Fig. 3 Cavitation erosion behavior of $Fe_{50}Mn_{30}Co_{10}Cr_{10}$ coating: (a) Cumulative volume loss; (b) Cavitation erosion rate; (c) Cumulative MDE; (d) MDER calculated in this work compared with data of other materials [6,8,14,36−40]

cumulative volume loss was about 55% less than that of $AlCoCr_xCuFe$ (x=2.0) coating. Compared with AISI 304 steel and $AlCoCr_xCuFe$ (x=2.0) coating, the incubation period of $Fe_{50}Mn_{30}Co_{10}Cr_{10}$ was longer, and the cavitation erosion rate remained less than 0.1 mm^3/h. Meanwhile, unlike AISI 304 steel and $AlCoCr_xCuFe$ (x=2.0) coating, which experienced a sharp increase in cavitation erosion rate within the first 5 h, $Fe_{50}Mn_{30}Co_{10}Cr_{10}$ coating experienced no acceleration period. Figure 3(c) presents the curves of cumulative MDE versus cavitation erosion time. It could be seen that unlike $FeCoCrAlNiTi_x$ (x=2.0) coating experiencing a rapid MDE increase after 6 h, the cumulative MDE of $Fe_{50}Mn_{30}Co_{10}Cr_{10}$ coating maintained slow growth. After 20 h, the cumulative MDE of $Fe_{50}Mn_{30}Co_{10}Cr_{10}$ coating was only 9% that of $FeCoCrAlNiTi_x$ (x=2.0) coating. Further, a comparative analysis (Fig. 3(d)) indicates that $Fe_{50}Mn_{30}Co_{10}Cr_{10}$ exhibited significantly high cavitation erosion resistance compared to various materials and protective coatings [6,8,14,36−40] commonly utilized in hydraulic machinery.

3.2 Microstructure and microhardness

Figure 4 displays the cross-sectional SEM micrograph of as-deposited $Fe_{50}Mn_{30}Co_{10}Cr_{10}$. It is obvious from Fig. 4(a) that the coating was well-formed. The cladding layer consisted of fine equiaxed crystals and columnar dendrites in different directions. Figure 4(b) presents detailed microstructure. It can be found that the as-deposited $Fe_{50}Mn_{30}Co_{10}Cr_{10}$ was composed of FCC γ phases and HCP ε phases, which was consistent with previous findings [32,33]. The HCP ε phase was removed by etching the matrix with $FeCl_3$ solution, and the granular HCP ε phase was observed to be embedded in the FCC γ phase matrix.

Figure 5 presents the XRD patterns of the as-deposited $Fe_{50}Mn_{30}Co_{10}Cr_{10}$ coating and the eroded coating after 20 h of cavitation erosion test, and both HCP ε and FCC γ phases were observed. Noticeably, after 20 h of cavitation erosion, the intensity of the diffraction peak of the FCC γ phase

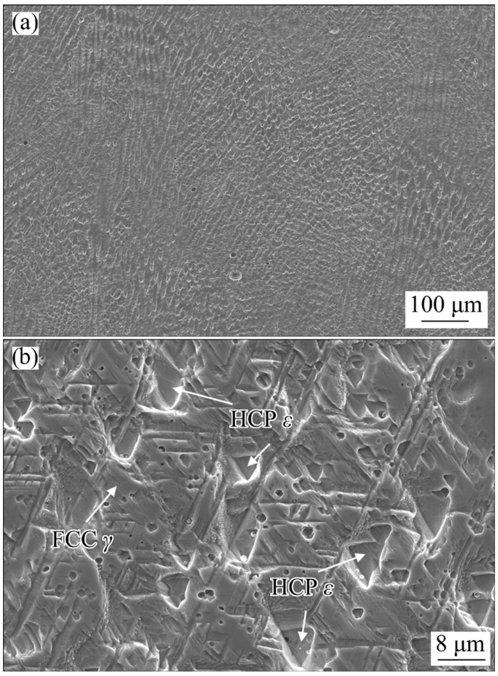

Fig. 4 Microstructures of as-deposited $Fe_{50}Mn_{30}Co_{10}Cr_{10}$ HEA on cross-section

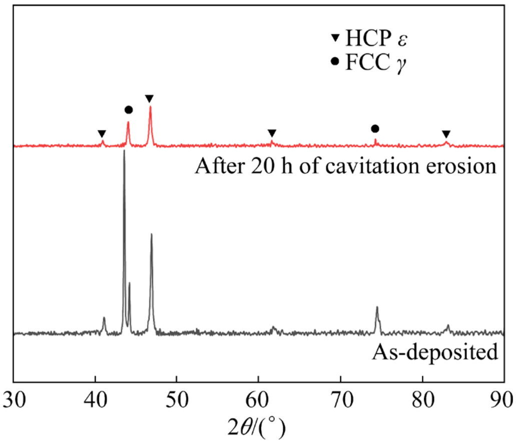

Fig. 5 XRD patterns of as-deposited $Fe_{50}Mn_{30}Co_{10}Cr_{10}$ coating and eroded coating after 20 h of cavitation erosion

decreased, while that of the HCP ε phase increased. These results indicated that the metastable FCC γ phase underwent a martensite transformation from FCC γ to the HCP ε phase during the cavitation erosion. This was mainly due to the repetitive impact of microjets and surge waves resulting from the implosion of vapor bubbles, which led to martensitic phase transformation. In the process of cavitation erosion, the instantaneous velocity of the high-speed micro-jet generated by the violent implosion of the micron-size vapor bubble inside the liquid can reach hundred meters per second, and the transient pressure can reach several GPa [3,41]. Under the frequent impact of the high-speed microjet and high stress, the surface of the sample had plastic deformation before it failed. Due to its TRIP property, the metastable phase FCC γ phase of $Fe_{50}Mn_{30}Co_{10}Cr_{10}$ experienced martensitic transformation to the HCP ε phase.

Figure 6 shows the EBSD analysis of the microstructure of $Fe_{50}Mn_{30}Co_{10}Cr_{10}$ coating after 20 h of cavitation erosion in distilled water. According to the phase map in Fig. 6(a), it could be seen that the surface structure of the sample was composed of FCC γ and HCP ε structure, which was consistent with the XRD results. The granular and massive HCP ε phases were embedded in the FCC γ matrix. It can be observed that many small pieces of HCP ε phase tended to accumulate and form many large pieces. Figure 6(b) shows the grain orientation of HEA coating. FCC γ large grains of the eroded sample exhibited mainly two orientation components: ⟨101⟩ (green) and close to ⟨001⟩. The grain orientation of the HCP ε phase was close to ⟨0001⟩. Compared with the EBSD analysis of $Fe_{50}Mn_{30}Co_{10}Cr_{10}$ in our previous studies [32], the content of FCC γ phase in HEA coating decreased from 88.7% to 61.2% after 20 h of cavitation erosion test, while the HCP ε phase content increased from 11.3% to 38.8% (Fig. 6(c)). It can be predicted that martensitic transformation has occurred in the cavitation erosion process. Under the impact of micro-jet, part of FCC γ phase transformed into HCP ε phase in the sample surface. As can be seen from Fig. 6(d), the average grain size increased to about 118 μm. Compared with as-deposited $Fe_{50}Mn_{30}Co_{10}Cr_{10}$ [32], the proportion of large grain size increased. This may be caused by the continuous aggregation and growth of the newly generated HCP ε phase due to martensitic transformation.

Figure 7(a) shows the variation of the microhardness of $Fe_{50}Mn_{30}Co_{10}Cr_{10}$ coating with cavitation erosion time. The surface microhardness increased from HV 270 to 410 after 20 h of test. The microhardness of the test specimen along the depth before and after 20 h of cavitation erosion test is shown in Fig. 7(b). It can be observed that the microhardness gradually decreased from the eroded surface along the depth direction to the level of the as-deposited $Fe_{50}Mn_{30}Co_{10}Cr_{10}$. The change of

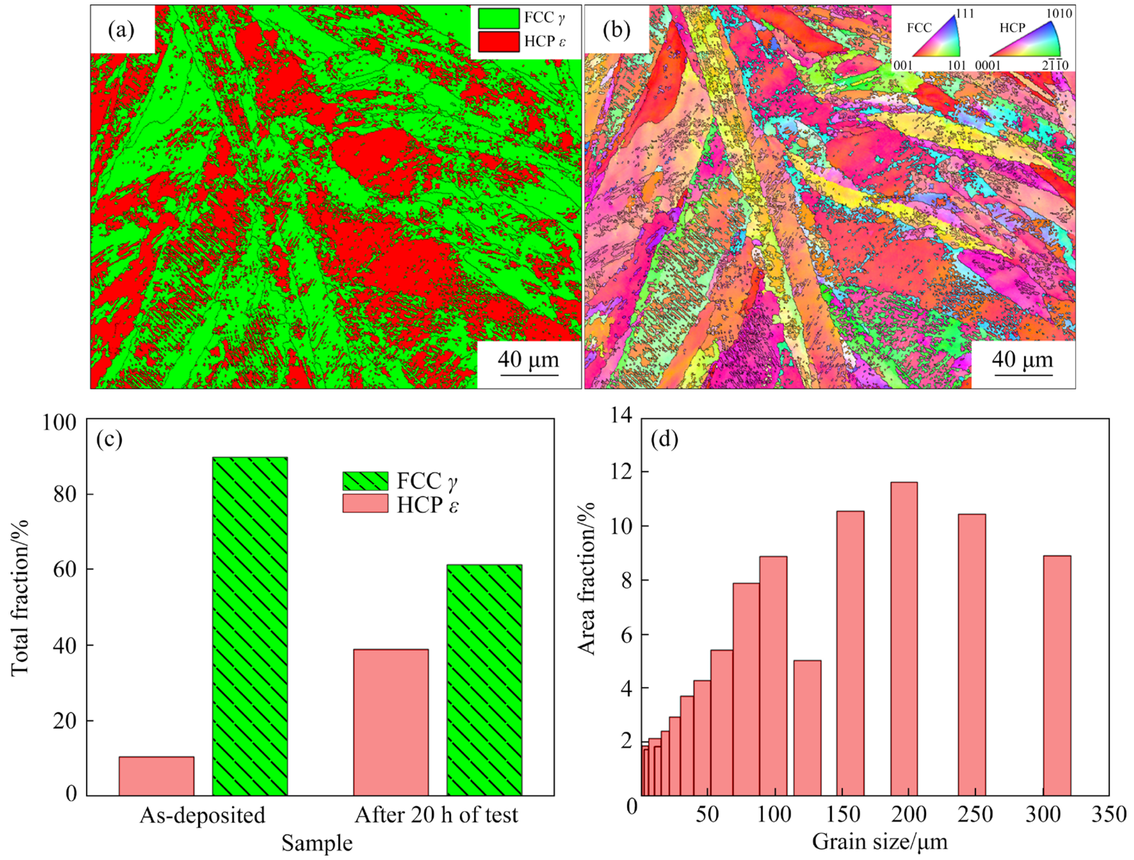

Fig. 6 EBSD analysis on $Fe_{50}Mn_{30}Co_{10}Cr_{10}$ coating after 20 h of cavitation erosion: (a) Phase map; (b) Inverse pole figure map; (c) Phase content; (d) Grain size distribution

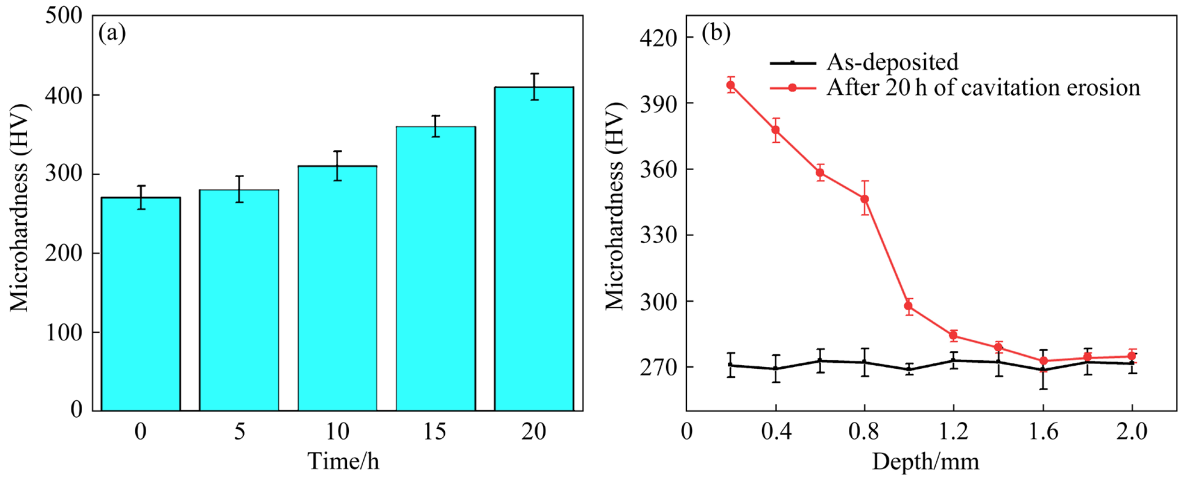

Fig. 7 Variation of microhardness of $Fe_{50}Mn_{30}Co_{10}Cr_{10}$ coating: (a) With cavitation erosion time; (b) Along depth

microhardness corresponded to the change of phase composition, which was investigated in XRD analysis. The HCP ε phase is harder than the FCC γ phase. Therefore, the increase in microhardness can be explained by the fact that with the evolution of cavitation erosion, the FCC γ phase underwent the martensitic transition and transformed to the HCP ε phase.

3.3 Cavitation erosion mechanisms

3.3.1 XPS analysis

According to the research of XU et al [16], XPS test can characterize the changes of compound states on the surface before and after cavitation erosion. To investigate the chemical composition on the surface of $Fe_{50}Mn_{30}Co_{10}Cr_{10}$ coating after 20 h of cavitation erosion, the XPS analysis (Fig. 8) was

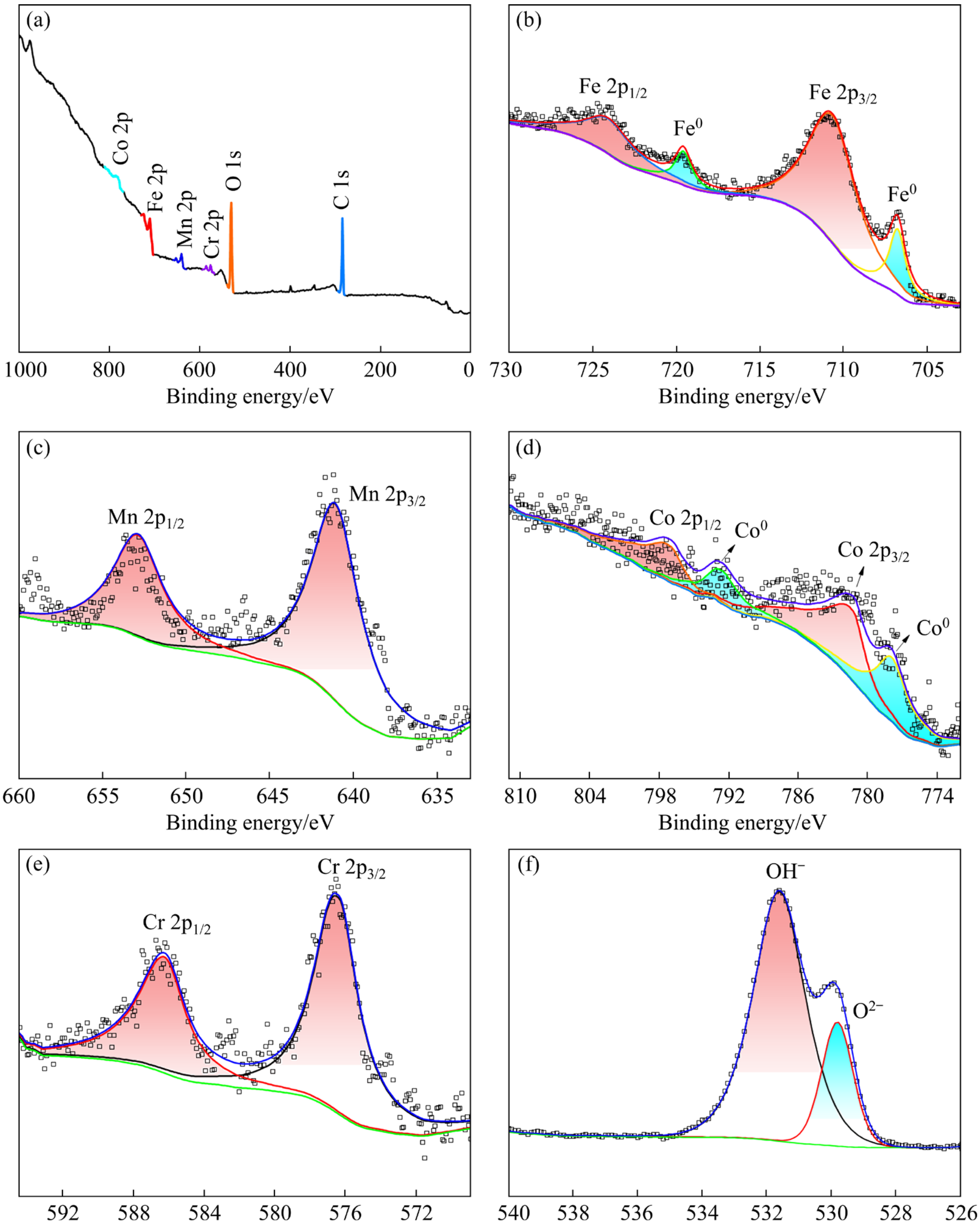

Fig. 8 XPS analysis of $Fe_{50}Mn_{30}Co_{10}Cr_{10}$ coating after 20 h of cavitation erosion: (a) XPS survey spectrum; (b−f) High-resolution XPS spectra assigned to Fe 2p, Mn 2p, Co 2p, Cr 2p and O 1s, respectively

performed on the eroded surface. In the XPS wide-scan survey spectrum (Fig. 8(a)), Fe 2p, Mn 2p, Co 2p, Cr 2p, O 1s and C 1s peaks were detected on the surface of the eroded coating. For the XPS Fe 2p spectrum (Fig. 8(b)), two prominent peaks located at binding energies of 711.1 and 724.6 eV were observed, corresponding to the binding energies for Fe $2p_{3/2}$ and Fe $2p_{1/2}$, respectively, which were consistent with the reported values for Fe_2O_3. Meanwhile, two slightly lower peaks could be observed at the binding energy of 706.7 and 719.8 eV, corresponding to the binding energy for Fe elemental metallic state [42,43]. It can be seen that stable Fe_2O_3 was formed by the partial oxidation of Fe elements in the $Fe_{50}Mn_{30}Co_{10}Cr_{10}$ coating during the cavitation erosion process. The XPS Mn 2p spectrum (Fig. 8(c)) consisted of one doublet peak at 641.4 and 653.1 eV, assigned to Mn $2p_{3/2}$ and Mn $2p_{1/2}$, respectively. These binding energies were close to the literature data for Mn in

Mn_2O_3 [44]. As shown in Fig. 8(d), the Co 2p spectrum was composed of two doublet peaks. One of the doublet peaks was from Co $2p_{3/2}$ and Co $2p_{1/2}$ located at 781.3 and 797.0 eV, respectively, corresponding to the binding energy of Co in stoichiometric Co_2O_3. And another doublet peak was at 777.3 and 792.4 eV, assigned to Co elemental metallic state [45]. The Cr 2p spectrum (Fig. 8(e)) consisted of a doublet peak at 576.7 and 586.7 eV, respectively, corresponding to Cr $2p_{3/2}$ and Cr $2p_{1/2}$ peaks, which was consistent with the Cr_2O_3 [46,47]. The asymmetric O 1s spectrum displayed in Fig. 8(f) could be divided into two components: one peak at 529.9 eV corresponding to O^{2-} in oxides, and another one at 531.7 eV corresponding to the bound water or adsorbed OH^- ions from the surrounding environment [16].

From the above analysis, it can be concluded that different oxides such as Fe_2O_3, Mn_2O_3, Co_2O_3, and Cr_2O_3 were generated on the eroded surface. In the cavitation erosion process, the violent implosion of the bubbles would not only produce instantaneous high-speed microjet and high stress, but also generate instantaneous high temperature in the bubble. According to the heat transfer model calculated by QIN and ALEHOSSEIN [48], when a cavitation bubble with an initial radius of 2 mm collapses, the maximum temperature of the air in the cavitation bubble can rise to more than 20000 K. Under the action of high-speed microjet, high stress and high temperature, the matrix elements on the surface reacted with the oxygen trapped in the bubbles to form various oxides. The stable hard oxides improved the surface hardness of the coating and delayed material shedding, thus improving the cavitation erosion resistance to a certain extent.

3.3.2 Cavitation erosion topography

To understand the failure mechanisms of $Fe_{50}Mn_{30}Co_{10}Cr_{10}$ coating during the cavitation erosion, the eroded surfaces were investigated by the SEM. Figure 9 presents the eroded surface morphologies of $Fe_{50}Mn_{30}Co_{10}Cr_{10}$ coating after cavitation erosion test for different exposure time in distilled water. As can be observed obviously from Figs. 9(a, b), after 5 h of test, some shallow wrinkles and local plastic deformations appeared at the delineated grain boundaries. The micro-cracks formed during this period due to plastic deformation became stress-concentrated areas, which functioned as the nucleation zones for later deep crater formation. As the test time increased to 10 h, the impact stress generated by the collapse of bubbles caused a small number of pits. Part of the material was removed, leading to roughened surfaces, as shown in Figs. 9(c, d). After a longer exposure time, the number and the size of craters and pits gradually increased, and adjacent craters merged into larger defects, leading to a large surface coating flake-off, as shown in Figs. 9(e, f). After 20 h of test (Figs. 9(g, h)), a large number of small pits and craters were formed in the interior of the specimen, and the specimen entered the stable damage stage, which exhibited a consistent pattern with the cavitation erosion rate curve in Fig. 3(b).

Figure 10 presents the 3D profile and 2D profile in horizontal (*A*), vertical (*B*) and oblique (*C*) directions of $Fe_{50}Mn_{30}Co_{10}Cr_{10}$ coating after 20 h of test. Under cavitation erosion damage, the surface material fell off to form the valley (blue area), and the plastic deformation produced the peak. It can be observed that there were few deep valleys, and most peaks were small. The distance between the peak and the valley of the eroded surface after 20 h test was within 30 μm.

The eroded surface roughness parameters are listed in Table 2. The measurements of surface roughness R_a reveal the level of surface damage. The R_p and R_v are the values of surface peak and valley respectively, and R_z is the sum of R_p and R_v. Among the three scanning directions, the *C* direction presented the highest peak and deepest valley, which were 5.613 μm and 12.94 μm, respectively. The values of R_a and R_z in different directions were less than 2.073 μm and 18.55 μm, respectively. The value of R_{sk} (skewness) describes the morphology of the height distribution and is sensitive to occasional deep valleys or high peaks. When the value of $R_{sk}>0$, it indicates that the material has a high peak count and is easily eroded by cavitation erosion. On the contrary, when $R_{sk}<0$, fewer peaks can be destroyed by cavitation erosion. The surface was prone to forming a water film, which played a buffering role in the cavitation erosion process [49]. As shown in Table 2, the R_{sk} values of the three scanning directions were all less than 0. This indicated that after 20 h of cavitation erosion, the peaks were less and a water film was generated on the surface. The specimen entered the stable damage stage with relatively slow mass loss.

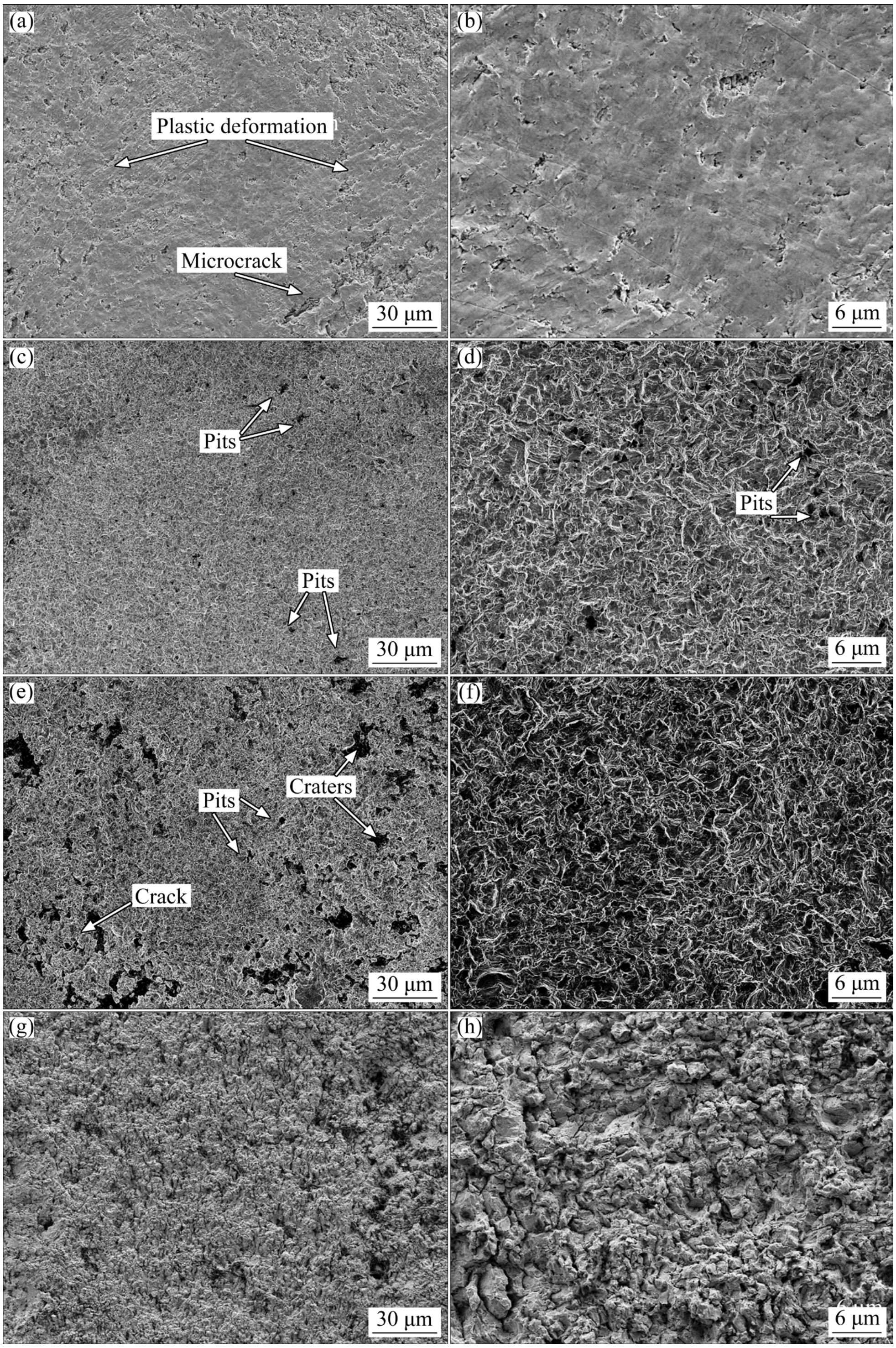

Fig. 9 SEM images of $Fe_{50}Mn_{30}Co_{10}Cr_{10}$ coating after cavitation erosion test for different time: (a, b) 5 h; (c, d) 10 h; (e, f) 15 h; (g, h) 20 h

3.3.3 Failure mechanisms

Figure 11 portrays the schematic diagram of the cavitation erosion failure mechanisms of the $Fe_{50}Mn_{30}Co_{10}Cr_{10}$ coating. During the first few hours of cavitation erosion, the surface of the sample was plastically deformed to produce shallow wrinkles and microcracks under the repeated impact of the high-speed microjet. Under ultrasonic excitation, the velocity of the cavitation bubbles can reach ~700 m/s [50], and the local pressure can reach 1.5 GPa [51]. The high-speed, high-intensity cavitation bubbles contributed to the

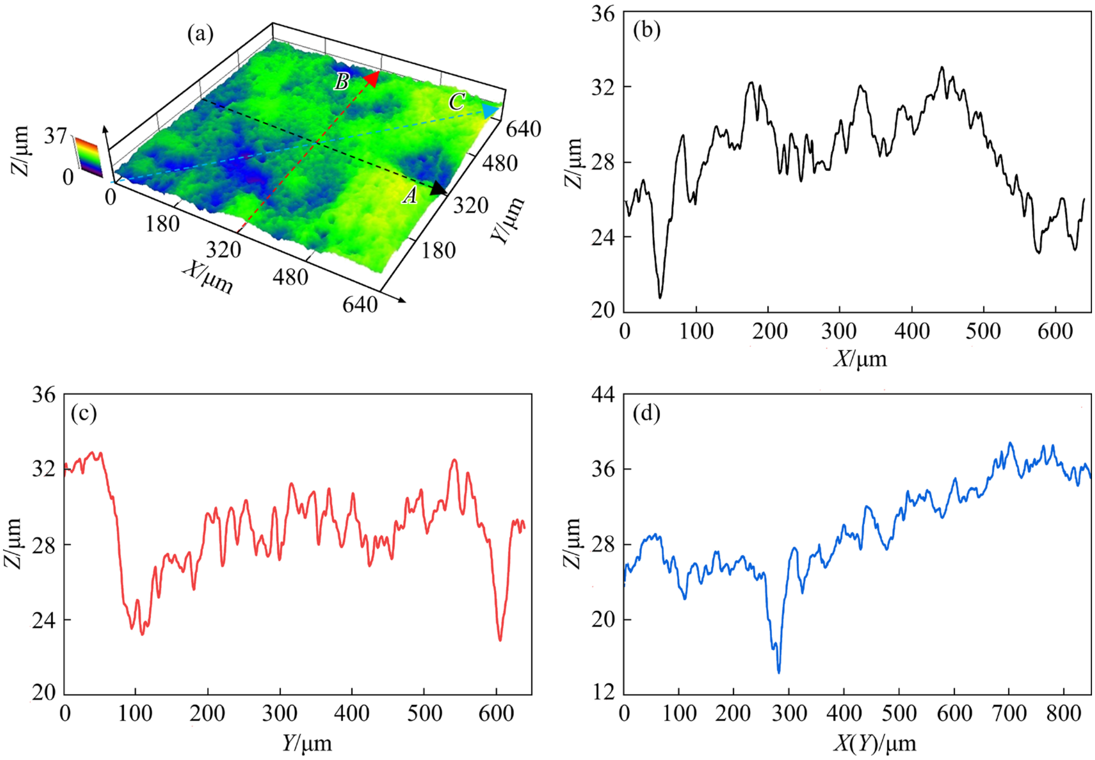

Fig. 10 Profiles of $Fe_{50}Mn_{30}Co_{10}Cr_{10}$ coating after 20 h of cavitation erosion: (a) 3D surface profile; (b) *A* direction; (c) *B* direction; (d) *C* direction

Table 2 Result of surface roughness after 20 h of cavitation erosion

Scanning direction	R_a/µm	R_p/µm	R_v/µm	R_z/µm	R_{sk}
A	2.073	4.718	7.534	12.25	−0.493
B	1.708	4.094	5.928	10.02	−0.479
C	1.853	5.613	12.94	18.55	−1.314

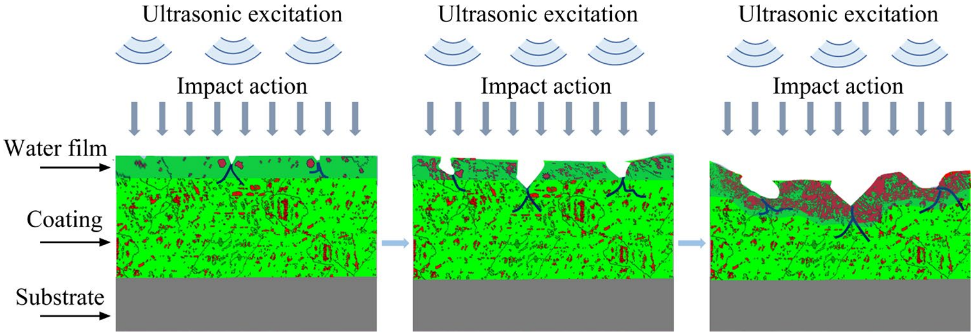

Fig. 11 Schematic diagram of cavitation erosion failure mechanisms of $Fe_{50}Mn_{30}Co_{10}Cr_{10}$ coating

plastic deformation of the material surfaces, and the micro-regions were subjected to great compressive stresses leading to the failure and the formation of pits.

Firstly, the TRIP effect of the $Fe_{50}Mn_{30}Co_{10}Cr_{10}$ was very helpful to enhance the work-hardening rate and postpone the onset of necking. Part of the FCC γ phase transformed into the HCP ε phase in the region where plastic deformation occurred. Local stress concentrations such as dislocation pile-ups, voids and FCC γ grain boundaries were favorable nucleation sites for HCP ε phase. Phase boundary propagation generated large amounts of dislocations entering into the FCC

γ matrix. Some dispersed HCP ε grains were converted from FCC γ grains. With the evolution of cavitation erosion, some craters and pits in the coating were formed due to plastic deformation. Afterwards, stress concentrations became more significant. The number of HCP ε grains rose rapidly. Meanwhile, the HCP ε grain area continued to aggregate and grow. The average grain size on the surface also increased. The FCC γ grains are known to be a soft phase with excellent elongation. However, the HCP ε as a hard phase has poor elongation. Therefore, with the progress of cavitation erosion, the strength and hardness of the test specimen surface were improved.

Secondly, complex microstructures could significantly enhance back stress strengthening and increase the resistance to cavitation erosion. Moving dislocation sources enabled plastic relaxation and prevent local damage accumulation caused by intense slipping in the FCC γ grains of the interfacial region. Geometrically necessary dislocations (GNDs) can synergize the strain field and thus increase the overall yield strength of the sample surface. At the same time, GNDs build up at the boundary in the FCC γ grains and cannot propagate across the boundary, resulting in high back stress [52−54]. In addition, the back-stress hardening effect caused by the non-homogeneous structure enhances the work-hardening ability and helps to maintain good ductility [53,55]. This enables the FCC γ zone to obtain almost the same strength as the HCP ε zone, resulting in a significant increase in the overall yield strength.

Finally, it could be seen that stable oxides such as Fe_2O_3, Mn_2O_3, Co_2O_3, and Cr_2O_3 were generated during cavitation erosion according to the results of XPS analysis. The stable hard oxides improved the cavitation erosion resistance to a certain extent by increasing the hardness to delay the material falling off. In addition, because the material fell off uniformly, the water film formed on the surface played a buffering role in the process of cavitation erosion.

In summary, the strength and plasticity of the sample surface were further enhanced during the onset of cavitation erosion. High strength–high ductility trade-off and stable hard oxides of the sample significantly delayed surface failure. After 20 h of cavitation erosion test, sample surface grains were uniformly exfoliated. But the sample maintained a low rate of failure throughout.

4 Conclusions

(1) After 20 h of cavitation erosion test, the cumulative volume loss of $Fe_{50}Mn_{30}Co_{10}Cr_{10}$ coating was approximately 55% less than that of $AlCoCr_xCuFe$ (x=2.0) coating, and the cumulative MDE was only 9% that of $FeCoCrAlNiTi_x$ (x=2.0) coating. The cavitation erosion resistance of the dual-phase $Fe_{50}Mn_{30}Co_{10}Cr_{10}$ HEA was superior to that of the single-phase $AlCoCr_xCuFe$ HEA.

(2) During the cavitation erosion process, the surface microstructure of $Fe_{50}Mn_{30}Co_{10}Cr_{10}$ coating underwent martensitic phase transformation by the action of a high-speed microjet. After 20 h of cavitation erosion testing, the amount of martensite HCP ε phase increased by a factor of 2.43, and surface hardness increased from HV 270 to HV 410.

(3) Due to TRIP effect of $Fe_{50}Mn_{30}Co_{10}Cr_{10}$, the HCP ε phase formed by the martensitic transformation continued to gather and grow to form flakes embedded in the FCC γ phase, producing back stress strengthening as well as process hardening effects. These effects effectively improved the cavitation erosion resistance. The stable oxides and water film formed in the cavitation erosion process delayed surface failure to a certain extent.

CRediT authorship contribution statement

Guo-cheng LIU: Conceptualization, Methodology, Project administration; **Jian-jiang LI:** Investigation, Formal analysis, Writing − Original draft; **Ning HU:** Investigation, Writing − Review & editing; **Qi-yong TU:** Data curation, Visualization, Writing − Review & editing; **Ze-qi HU:** Data curation, Funding acquisition; **Lin HUA:** Resources, Project administration.

Declaration of competing interest

The authors declare that they have no known competing financial interests or personal relationships that could have appeared to influence the work reported in this paper.

Acknowledgments

This work was financially supported by the Innovative Research Team Development Program of Ministry of Education of China (No. IRT_17R83), and State Key Laboratory of Materials Processing and Die &

Mould Technology, Huazhong University of Science and Technology, China (No. P2021-018).

References

[1] LUO Xian-wu, JI B, TSUJIMOTO Y. A review of cavitation in hydraulic machinery [J]. Journal of Hydrodynamics, 2016, 28(3): 335−358.

[2] SINGH R, TIWARI S K, MISHRA S K. Cavitation erosion in hydraulic turbine components and mitigation by coatings: Current status and future needs [J]. Journal of Materials Engineering and Performance, 2011, 21(7): 1539−1551.

[3] BAKHSHANDEH H R, ALLAHKARAM S R, ZABIHI A H. An investigation on cavitation-corrosion behavior of Ni/beta-SiC nanocomposite coatings under ultrasonic field [J]. Ultrason Sonochem, 2019, 56: 229−239.

[4] BASUMATARY J, WOOD R J K. Different methods of measuring synergy between cavitation erosion and corrosion for nickel aluminium bronze in 3.5% NaCl solution [J]. Tribology International, 2020, 147: 104843.

[5] TANG C H, CHENG F T, MAN H C. Laser surface alloying of a marine propeller bronze using aluminium powder [J]. Surface and Coatings Technology, 2006, 200(8): 2602−2609.

[6] SAENZ-BETANCOURT C C, RODRíGUEZ S A, CORONADO J J. Effect of boronising on the cavitation erosion resistance of stainless steel used for hydromachinery applications [J]. Wear, 2022, 498/499: 204330.

[7] WANG Chang-chang, TAN Lei, CHEN Men-di, FAN Hong-gang, LIU De-ming. A review on synergy of cavitation and sediment erosion in hydraulic machinery [J]. Frontiers in Energy Research, 2022, 10: 1047984.

[8] WU C L, ZHANG S, ZHANG C H, ZHANG H, DONG S Y. Phase evolution and cavitation erosion-corrosion behavior of FeCoCrAlNiTi_x high entropy alloy coatings on 304 stainless steel by laser surface alloying [J]. Journal of Alloys and Compounds, 2017, 698: 761−770.

[9] ZHANG S, WU C L, ZHANG C H, GUAN M, TAN J Z. Laser surface alloying of FeCoCrAlNi high-entropy alloy on 304 stainless steel to enhance corrosion and cavitation erosion resistance [J]. Optics & Laser Technology, 2016, 84: 23−31.

[10] MITELEA I, DIMIAN E, BORDEASU I, CRACIUNESCU C. Ultrasonic cavitation erosion of gas nitrided Ti−6Al−4V alloys [J]. Ultrason Sonochem, 2014, 21: 1544−1548.

[11] CIUBOTARIU C R, SECOSAN E, MARGINEAN G, FRUNZAVERDE D, CAMPIAN V C. Experimental study regarding the cavitation and corrosion resistance of stellite 6 and self-fluxing remelted coatings [J]. Strojniški Vestnik - Journal of Mechanical Engineering, 2016, 62(3): 154−162.

[12] HONG Sheng, WU Yu-ping, ZHANG Jian-feng, ZHENG Yu-gui, ZHENG Yuan, LIN Jin-ran. Synergistic effect of ultrasonic cavitation erosion and corrosion of WC−CoCr and FeCrSiBMn coatings prepared by HVOF spraying [J]. Ultrason Sonochem, 2016, 31: 563−569.

[13] QIAO Lei, WU Yu-ping, HONG Sheng, ZHANG Jian-feng, SHI Wei, ZHENG Yu-gui. Relationships between spray parameters, microstructures and ultrasonic cavitation erosion behavior of HVOF sprayed Fe-based amorphous/nanocrystalline coatings [J]. Ultrason Sonochem, 2017, 39: 39−46.

[14] NAIR R B, ARORA H S, MUKHERJEE S, SINGH S, SINGH H, GREWAL H S. Exceptionally high cavitation erosion and corrosion resistance of a high entropy alloy [J]. Ultrason Sonochem, 2018, 41: 252−260.

[15] BAO Ye-feng, GUO Lin-po, ZHONG Chong-hui, SONG Qi-ning, YANG Ke, JIANG Yong-feng, WANG Zi-rui. Effects of WC on the cavitation erosion resistance of FeCoCrNiB0.2 high entropy alloy coating prepared by laser cladding [J]. Materials Today Communications, 2021, 26: 102154.

[16] XU Jiang, PENG Shuang, LI Zhang-yang, JIANG Shu-yun, XIE Zong-han, MUNROE P, LU Hong. Remarkable cavitation erosion–corrosion resistance of CoCrFeNiTiMo high-entropy alloy coatings [J]. Corrosion Science, 2021, 190: 109663.

[17] ZENG Si-qi, TIAN Jing-jing, HU Shu-bing, XIAO Ming, PENG Bo. Effect of laser surface melting on microstructure evolution and cavitation behavior of nickel aluminum bronze [J]. Transactions of Nonferrous Metals Society of China, 2023, 33(7): 2090−2109.

[18] DING Xiang, KE Du, YUAN Cheng-qing, DING Zhang-xiong, CHENG Xu-dong. Microstructure and cavitation erosion resistance of HVOF deposited WC−Co coatings with different sized WC [J]. Coatings, 2018, 8(9): 307.

[19] KRELLA A. The influence of TiN coatings properties on cavitation erosion resistance [J]. Surface and Coatings Technology, 2009, 204(3): 263−270.

[20] KRELLA A K, CZYZNIEWSKI A, GILEWICZ A, GAJOWIEC G. Experimental study of the influence of deposition of multilayer CrN/CrCN PVD coating on austenitic steel on resistance to cavitation erosion [J]. Coatings, 2020, 10(5): 487.

[21] LIU Zheng-liang, KHAN A, SHEN Ming-li, ZHU Sheng-long, ZENG Chao-liu, WANG Fu-hui, FU Chao. Microstructure and cavitation erosion resistance of arc ion plating NiCrAlY coating on the 304L stainless steel [J]. Tribology International, 2022, 173: 107618.

[22] CANTOR B, CHANG I T H, KNIGHT P, VINCENT A J B. Microstructural development in equiatomic multicomponent alloys [J]. Materials Science and Engineering A, 2004, 375/376/377: 213−218.

[23] TSAI M H, YEH J W. High-entropy alloys: A critical review [J]. Materials Research Letters, 2014, 2(3): 107−123.

[24] LI Zhi-ming, PRADEEP K G, DENG Yun, RAABE D, TASAN C C. Metastable high-entropy dual-phase alloys overcome the strength−ductility trade-off [J]. Nature, 2016, 534(7606): 227−230.

[25] ARIF Z U, KHALID M Y, AL RASHID A, UR REHMAN E, ATIF M. Laser deposition of high-entropy alloys: A comprehensive review [J]. Optics & Laser Technology, 2022, 145: 107447.

[26] TIAN Yu-sheng, ZHOU Wen-zhe, TAN Qing-biao, WU Ming-xu, QIAO Shen, ZHU Guo-liang, DONG An-ping, SHU Da, SUN Bao-de. A review of refractory high-entropy alloys [J]. Transactions of Nonferrous Metals Society of China, 2022, 32(11): 3487−3515.

[27] SENKOV O N, WOODWARD C F. Microstructure and properties of a refractory NbCrMo0.5Ta0.5TiZr alloy [J]. Materials Science and Engineering A, 2011, 529: 311−320.

[28] YU P F, ZHANG L J, CHENG H, ZHANG H, MA M Z, LI Y C, LI G, LIAW P K, LIU R P. The high-entropy alloys with high hardness and soft magnetic property prepared by mechanical alloying and high-pressure sintering [J]. Intermetallics, 2016, 70: 82−87.

[29] LÖBEL M, LINDNER T, MEHNER T, LAMPKE T. Microstructure and wear resistance of AlCoCrFeNiTi high-entropy alloy coatings produced by HVOF [J]. Coatings, 2017, 7(9): 144.

[30] POLETTI M G, FIORE G, GILI F, MANGHERINI D, BATTEZZATI L. Development of a new high entropy alloy for wear resistance: FeCoCrNiW0.3 and FeCoCrNiW0.3+ 5 at.% of C [J]. Materials & Design, 2017, 115: 247−254.

[31] TANG Zhi, HUANG Lu, HE Wei, LIAW P. Alloying and processing effects on the aqueous corrosion behavior of high-entropy alloys [J]. Entropy, 2014, 16(2): 895−911.

[32] SUN Ming, LIU Guo-cheng, WEI Wen-ting, ZHOU Ling-yun, LI Jian-jiang, TU Qi-yong. Microstructures, mechanical and high-temperature tribological properties of dual-phase Fe50Mn30Co10Cr10 high-entropy alloy fabricated by laser metal deposition [J]. JOM, 2023, 75: 4138−4149.

[33] LI Zhi-ming, TASAN C C, PRADEEP K G, RAABE D. A TRIP-assisted dual-phase high-entropy alloy: Grain size and phase fraction effects on deformation behavior [J]. Acta Materialia, 2017, 131: 323−335.

[34] NIU Peng-da, LI Rui-di, FAN Zhi-qi, YUAN Tie-chui, ZHANG Zhi-jiang. Additive manufacturing of TRIP-assisted dual-phases Fe50Mn30Co10Cr10 high-entropy alloy: Microstructure evolution, mechanical properties and deformation mechanisms [J]. Materials Science and Engineering A, 2021, 814: 141264.

[35] YIN Dang-qing, LIANG Guang-bing, FAN Shuai, LI Shan-xin. Ultrasonic cavitation erosion behavior of AlCoCr$_x$CuFe high entropy alloy coatings synthesized by laser cladding [J]. Materials, 2020, 13(18): 4067.

[36] JIANG G B, ZHENG Y K, YANG Y Y, FANG H S. Caviation erosion of bainitic steel [J]. Wear, 1998, 215: 46−53.

[37] DI V.CUPPARI M G, SOUZA R M, SINATORA A. Effect of hard second phase on cavitation erosion of Fe−Cr−Ni−C alloys [J]. Wear, 2005, 258: 596−603.

[38] TAILLON G, POUGOUM F, LAVIGNE S, TON-THAT L, SCHULZ R, BOUSSER E, SAVOIE S, MARTINU L, KLEMBERG-SAPIEHA J E. Cavitation erosion mechanisms in stainless steels and in composite metal–ceramic HVOF coatings [J]. Wear, 2016, 364/365: 201−210.

[39] OLIVEIRA D B, FRANCO A R, BOZZI A C. Influence of low temperature plasma carbonitriding on cavitation erosion resistance of the Stellite 250 alloy – A preliminary evaluation [J]. Wear, 2021, 476: 203653.

[40] ROA C V, VALDES J A, LARRAHONDO F, RODRÍGUEZ S A, CORONADO J J. Comparison of the resistance to cavitation erosion and slurry erosion of four kinds of surface modification on 13-4 Ca6NM hydro-machinery steel [J]. Journal of Materials Engineering and Performance, 2021, 30(10): 7195−7212.

[41] KRELLA A K. Degradation and protection of materials from cavitation erosion: A review [J]. Materials (Basel), 2023, 16(5): 2058.

[42] TAN B J, KLABUNDE K J, SHERWOOD P M A. X-ray photoelectron spectroscopy studies of solvated metal atom dispersed catalysts: Monometallic iron and bimetallic iron-cobalt particles on alumina [J]. Chemistry of Materials, 1990, 2(2): 186−191.

[43] YAMASHITA T, HAYES P. Analysis of XPS spectra of Fe^{2+} and Fe^{3+} ions in oxide materials [J]. Applied Surface Science, 2008, 254: 2441−2449.

[44] ILTON E S, POST J E, HEANEY P J, LING F T, KERISIT S N. XPS determination of Mn oxidation states in Mn (hydr)oxides [J]. Applied Surface Science, 2016, 366: 475−485.

[45] TAN B J, KLABUNDE K J, SHERWOOD P M A. XPS studies of solvated metal atom dispersed (SMAD) catalysts. Evidence for layered cobalt-manganese particles on alumina and silica [J]. Journal of the American Chemical Society, 1991, 113(3): 855−861.

[46] SALVI A M, CASTLE J E, WATTS J F, DESIMONI E. Peak fitting of the chromium 2p XPS spectrum [J]. Applied Surface Science, 1995, 90(3): 333−341.

[47] DESIMONI E, MALITESTA C, ZAMBONIN P G, RIVIÈRE J C. An X-ray photoelectron spectroscopic study of some chromium−oxygen systems [J]. Surface and Interface Analysis, 1988, 13(2/3): 173−179.

[48] QIN Z, ALEHOSSEIN H. Heat transfer during cavitation bubble collapse [J]. Applied Thermal Engineering, 2016, 105: 1067−1075.

[49] WANG L, MAO J, XUE C, GE H, DONG G, ZHANG Q, YAO J. Cavitation-erosion behavior of laser cladded low-carbon cobalt-based alloys on 17-4PH stainless steel [J]. Optics & Laser Technology, 2023, 158: 108761.

[50] LI D G, WANG J D, CHEN D R, LIANG P. Ultrasonic cavitation erosion of Ti in 0.35% NaCl solution with bubbling oxygen and nitrogen [J]. Ultrason Sonochem, 2015, 26: 99−110.

[51] DULAR M, BACHERT B, STOFFEL B, ŠIROK B. Relationship between cavitation structures and cavitation damage [J]. Wear, 2004, 257: 1176−1184.

[52] WU Xiao-lei, ZHU Yun-tian. Heterogeneous materials: A new class of materials with unprecedented mechanical properties [J]. Materials Research Letters, 2017, 5(8): 527−532.

[53] YANG Guang-hui, KIM J K. Hierarchical precipitates, sequential deformation-induced phase transformation, and enhanced back stress strengthening of the micro-alloyed high entropy alloy [J]. Acta Materialia, 2022, 233: 117974.

[54] HU C, HUANG C P, LIU Y X, PERLADE A, ZHU K Y, HUANG M X. The dual role of TRIP effect on ductility and toughness of a medium Mn steel [J]. Acta Materialia, 2023, 245: 118629.

[55] LIU X L, XUE Q Q, WANG W, ZHOU L L, JIANG P, MA H S, YUAN F P, WEI Y G, WU X L. Back-stress-induced strengthening and strain hardening in dual-phase steel [J]. Materialia, 2019, 7: 100376.

激光熔化沉积 $Fe_{50}Mn_{30}Co_{10}Cr_{10}$ 高熵合金涂层的空蚀行为

刘国承[1,2,3]，李建江[1,2,3]，胡 宁[1,2,3]，涂其勇[1,2,3]，胡泽启[1,2,3]，华 林[1,2,3]

1. 武汉理工大学 现代汽车零部件技术湖北省重点实验室，武汉 430070；
2. 武汉理工大学 汽车零部件技术湖北省协同创新中心，武汉 430070；
3. 武汉理工大学 汽车工程学院，武汉 430070

摘 要：为了揭示激光熔化沉积技术制备的 $Fe_{50}Mn_{30}Co_{10}Cr_{10}$ 涂层的空蚀机理，对涂层的相组成演变、显微组织、显微硬度、耐空蚀性和失效机理进行了研究。结果表明：在蒸馏水中进行 20 h 空蚀测试后，涂层表面的马氏体 HCP ε 相增加了 2.43 倍，显微硬度由 HV 270 提高到 HV 410。表面累积体积损失相比 $AlCoCr_xCuFe$ (x=2.0)涂层减少 55%，累积平均侵蚀深度仅为 $FeCoCrAlNiTi_x$ (x=2.0)涂层的 9%。由于非均质组织引起的背应力强化和加工硬化，涂层的表面强度和塑性在空蚀过程中得到进一步加强，有效提高了涂层的耐空蚀性能。

关键词：空蚀；$Fe_{50}Mn_{30}Co_{10}Cr_{10}$ 高熵合金；相变诱导塑性；激光熔化沉积；失效机理

(Edited by Bing YANG)